NANO LETTERS

pubs.acs.org/NanoLett Letter

Nanoscale Optical Conductivity Imaging of Double-Moiré Twisted Bilayer Graphene

Songbin Cui, Chengxin Jiang, Zhen Zhan, Ty Wilson, Naipeng Zhang, Xiaoming Xie, Shengjun Yuan, Haomin Wang,* Cyprian Lewandowski, and Guangxin Ni*

Cite This: *Nano Lett.* 2024, 24, 11490−11496 Read Online

ACCESS | Metrics & More | Article Recommendations | Supporting Information

ABSTRACT: A central paradigm of moiré materials relies on the formation of superlattices that yield enlarged effective crystal unit cells. While a critical consequence of this phenomenon is the celebrated flat electronic bands that foster strong interaction effects, the presence of superlattices has further implications. Here we explore the advantages of moiré superlattices in twisted bilayer graphene (TBG) aligned with hexagonal boron nitride (hBN) for passively enhancing optical conductivity in the low-energy regime. To probe the local optical response of TBG/hBN double-moiré lattices, we use infrared (IR) nano-imaging in conjunction with nanocurrent imaging to examine local optical conductivity over a wide range of TBG twist angles. We show that interband transitions associated with the multiple moiré flat and dispersive bands produce tunable transparent IR responses even at finite carrier densities, which is in stark contrast to the previously limited metallic near transparency observed only in undoped pristine graphene.

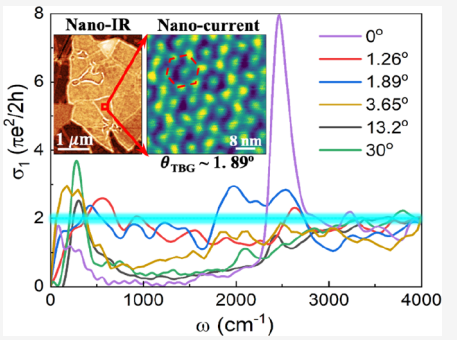

KEYWORDS: *double-moiré materials, plasmon polaritons, nano-infrared imaging, nanocurrent imaging, moiré optoelectronics*

Downloaded via FLORIDA STATE UNIV on January 29, 2025 at 17:46:00 (UTC).
See https://pubs.acs.org/sharingguidelines for options on how to legitimately share published articles.

In twisted bilayer graphene (TBG), the moiré lattice is formed by overlapping two graphene sheets with a slight rotational misalignment, creating an approximately periodic pattern of carbon atoms from the two consecutive layers. This moiré pattern results in an effective enlarged unit cell, which mathematically translates to the appearance of a smaller moiré Brillouin zone (mBZ). As a result, the Dirac cone linear dispersions in both graphene layers become folded and hybridized, yielding a dense multiband electronic spectrum.[1−3] This spectrum hosts two flat bands where the scale of electronic interactions is comparable to the electron kinetic energy, leading to exotic new phases ranging from correlated insulating states to superconductivity.[4,5] However, the impact of the superlattice on the electronic properties of moiré systems goes beyond the formation of flat bands, yielding enhanced optoelectronic properties, as we demonstrate in this work.

To further explore the interplay of moiré lattice formation on the electronic degrees of freedom, we constructed our system to possess two interwoven moiré lattices. Upon introduction of an additional degree of freedom into the TBG moiré system, namely the second twist angle in multilayer van der Waals (vdW) heterostructure, recent studies[3,6−10] have uncovered new phenomena arising from the enhanced control over electronic phases and correlations. One of the prominent examples is magic angle TBG (MATBG) aligned with hexagonal boron nitride (hBN), resulting in the formation of a double-moiré structure.[3,7] This double moiré, or moiré of moiré heterostructures, exhibits entirely new physics, as evidenced by the discovery of phenomena, including the quantum anomalous Hall effect (QAHE) and ferromagnetism.[11,12] These groundbreaking studies have shed light on the unique properties and exciting possibilities offered by such intricate layered systems.

To date, experimental evidence for the moiré phenomena is predominantly investigated through electrical transport or local density of states probe measurements.[3−5,13,14] However, only recently have optical excitations and electronic collective modes present in magic angle moiré systems started to be explored.[15,16] The quest for thoroughly examining these phenomena using conventional optical means is exacerbated by the small device area (sub-square micrometers) of moiré domains that are often in the proximity of other domains and twist angles[17] (Figure 1). To alleviate this problem, we employ two complementary imaging techniques: scattering-type scanning near-field optical microscopy (s-SNOM)[15,18−21] and vertical conductivity current imaging using conductive atomic force microscopy (c-AFM).[7,22] s-SNOM allows the probing of local optical conductivity and launching surface plasmons,

Received: June 16, 2024
Revised: August 27, 2024
Accepted: August 28, 2024
Published: September 3, 2024

ACS Publications © 2024 American Chemical Society

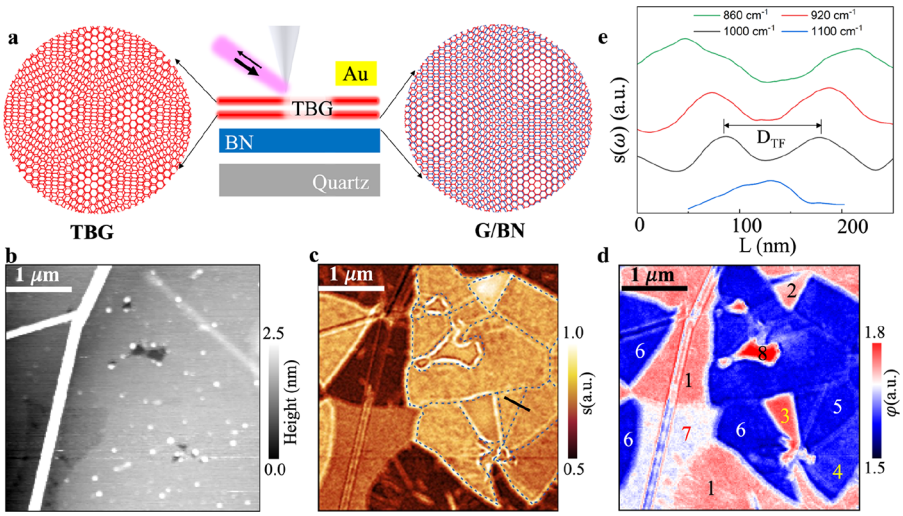

Figure 1. Nano-IR probing of a TBG/hBN crystal with different twist angles. (a) Schematic of the near-field imaging of TBG/hBN with two sets of moiré patterns. (b) AFM topography image, where the bright lines are the wrinkles from the underlying hBN flakes. (c and d) Near-field amplitude s and phase φ images plotted in real space at an IR frequency of 1000 cm^{-1} (~124 meV). In panel c, the black line represents the line-cut position, as shown in panel e. The blue dashed lines delineate the boundaries between different TBG domains. In panel d, different numbers mark different moiré superlattice regions. (e) Plasmon line profile dispersion across a domain boundary between regions with different twist angles. See the details below and in the Supporting Information.

enabling experimental access to the electronic structure and electron−hole excitations in moiré domains within 20 nm spatial resolutions.[23,24] Meanwhile, c-AFM with atomic resolution assists in uncovering the real-space moiré superlattice structures,[25] allowing us to precisely determine the twist angles and elucidate the lattice relaxation effects. We emphasize the ability to examine the same regions inside the same sample by harnessing multimessenger observations (s-SNOM, c-AFM, and AFM) to formulate a new strategy for unambiguously revealing the local electronic and optical responses of moiré systems.[17,26,27]

Our TBG microcrystals were grown by chemical vapor deposition (CVD) on top of hBN/quartz[7,22] (see the Supporting Information). The key advantage of this synthesis approach over the commonly used tear-and-stack method[3,11,12,15] is the generation of a large number of TBG domains with a wide range of twist angles θ_{TBG} naturally occurring within a single flake, which offers a unique platform for interrogating the twist angle dependence of TBG (Figure 1). Simultaneously, the bottom graphene layer is aligned with respect to the underlying hBN lattice, yielding a G/hBN moiré pattern with a twist angle $\theta_{G/hBN}$ close to 0°. In such a TBG/hBN moiré structure, the two consecutive twist angles, θ_{TBG} and $\theta_{G/hBN}$, give rise to periodic beating on different length scales that can be investigated within the field of view (FOV). The effective interplay of θ_{TBG} and $\theta_{G/hBN}$ thus offers peculiar double-moiré[28−30] structures with spatially variable TBG twist angles superimposed over fixed G/hBN lattices, a system that remains completely unexplored experimentally in the optical domain.

We begin by describing the nano-infrared (nano-IR) imaging results of local optical conductivity and plasmons in TBG/BN double-moiré structures using the s-SNOM apparatus (Figure 1a). In our experiments, a metalized tip of an atomic force microscope was illuminated by IR light at a frequency ω of $1/\lambda_0$, where λ_0 is the incident photon wavelength. This antenna-based nano-IR setup circumvents the TBG's momentum mismatch between incident photons and surface plasmons.[15,17,25] By using an interferometric detection method,[31−33] we simultaneously obtain scattered near-field amplitude $s(\omega)$ and its phase $\phi(\omega)$. These two quantities uniquely reveal local variations of complex optical conductivity $\sigma(\omega)$ and elucidate plasmon properties when light frequency ω falls within the plasmon excitation energy range. Specifically, the detected near-field signal is governed by the plasmon complex momentum $q_p \sim \{i\omega[1 + \varepsilon_{sub}(\omega)]\}/4\pi\sigma(\omega)$, where $\sigma(\omega) = \sigma_1(\omega) + i\sigma_2(\omega)$ is the complex optical conductivity of TBG/hBN and $\varepsilon_{sub}(\omega)$ is the known dynamical dielectric function of the substrate.[34] Because the optical conductivity reflects the underlying electronic band structure, the obtained nano-IR signal enables us to determine the specific twist angles of each domain and unravel the detailed microscopic description of the double-moiré lattice structures, as detailed below.

Panels c and d of Figure 1 show typical nano-IR imaging results. Here we plot raster-scanned images of the normalized near-field signal at a selected IR frequency ω of 1000 cm^{-1} (~124 meV). Adjacent multiple TBG regions with different twist angles θ_{TBG}, as well as G/hBN domains with fixed angles $\theta_{G/hBN}$, are captured within the same FOV, an experimental advantage that has allowed us to examine the impact of double-moiré lattices within the same microcrystal. The most prominent aspect of the images in panels c and d of Figure 1 is the distinct near-field signal ("contrast") observed between each of the TBG/hBN domains. For instance, submicrometer-sized commensurate moiré domain regions 1 and 4 show suppressed near-field amplitude (lower σ_1), while regions 2 and 3 display enhanced near-field signals (larger σ_1). By corroborating with the topography AFM image (Figure 1b), we identify region 7 as G/hBN and region 8 as the hBN/quartz substrate (see section 2 of the Supporting Information). Additionally, plasmonic fringe patterns emerge at each domain boundary. Figure 1e shows the extracted plasmonic line profile from the region marked in Figure 1c. These fringe patterns are attributed to plasmons propagating waves in TBG/hBN and being reflected by the TBG boundary. Specifically, the

https://doi.org/10.1021/acs.nanolett.4c02841
Nano Lett. 2024, 24, 11490−11496

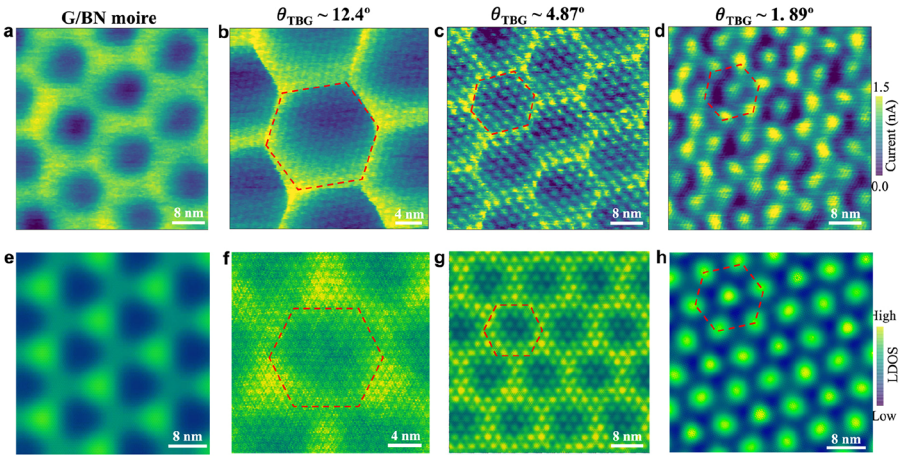

Figure 2. Nanocurrent images with varying twist angles. Experimentally measured current images on TBG/hBN at variable TBG twist angles θ_{TBG}, including (a) 0°, (b) 12.4°, (c) 4.87°, and (d) 1.89°. During nanocurrent measurements, a constant bias was applied between the conductive tip and the bottom graphene flake. (e−h) Theoretically simulated current images showing the local density of states of TBG/hBN at the same θ_{TBG} values as shown in panels a−d, respectively. The agreement of theoretically calculated nanocurrent images with the experimental results confirms the validity of the microscopic modeling.

a

	Moiré type	$\theta_{G/G}$	$\theta_{G/hBN}$
1	TBG/hBN	0°	0°
2	TBG/hBN	1.26°	0°
3	TBG/hBN	1.89°	0°
4	TBG/hBN	4.87°	0°
5	TBG/hBN	12.4°	0°
6	TBG/hBN	30°	0°
7	G/hBN	N.A.	0°
8	hBN	N.A.	N.A.
9	TBG/hBN	3.65°	0°

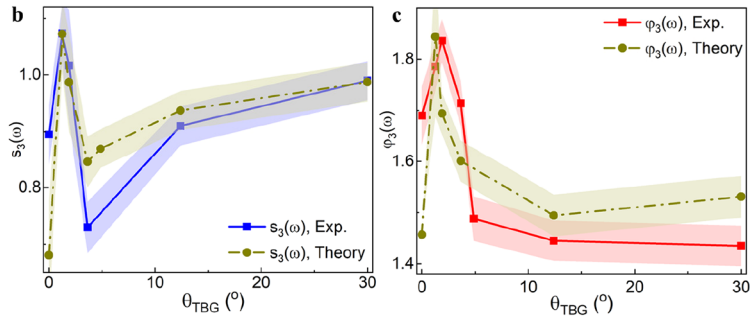

Figure 3. Extraction of the near-field optical signal as a function of θ_{TBG}. (a) Illustration of variable twisted regimes under study. (b) Comparison of the experimentally extracted and theoretically calculated near-field amplitude as a function of θ_{TBG}. (c) Comparison of the experimentally extracted and theoretically calculated near-field phase as a function of θ_{TBG} (details in the text and Supporting Information).

observed twin fringe plasmon wavelength decreases monotonically, as the incident light frequency varies from 860 to 1100 cm^{-1}. Such systematic variation of the plasmon wavelength and the corresponding real part of plasmon wave vector $q_1(\omega)$ yield a plasmon dispersion for the collective excitations with a positive group velocity. Analyzing the wavelength of the plasmonic fringes in the G/hBN region allows us to estimate the chemical potential in the device. In short, the plasmon wavelength analysis indicates that the samples under study are moderately hole-doped with a Fermi energy (E_F) of approximately −150 meV (see section 5 of the Supporting Information).

Before delving into a detailed analysis of the optical conductivity in each region, we take a moment to closely examine the atomic structure of each labeled TBG/hBN double-moiré domain in Figure 1 and validate our microscopic modeling. This is accomplished by employing c-AFM, in which a constant bias voltage is applied between the metallic atomic force microscope tip and TBG flakes. This setup enables us to continuously monitor the nanocurrent, which is proportional to the local density of states in real space, with a remarkable resolution of ∼1 nm. Such a precise procedure empowers us to accurately determine both the moiré wavelength (λ_m) and the corresponding TBG and G/hBN twist angles.[7,22]

Panels a−d of Figure 2 show the real-space nanocurrent imaging obtained from various domains as labeled in Figure 1d. In the cases in which θ_{TBG} is either 0° (labeled in region 1, Bernal AB stacked) or close to 30° (marked in region 6), the corresponding TBG moiré patterns will not be distinguishable (see section 3 of the Supporting Information). Therefore, we observe a single set of moiré patterns arising from the G/hBN interface with a honeycomb moiré lattice structure, as shown in Figure 2a. As θ_{TBG} approaches 12.4° (Figure 2b, corresponding to region 5 in Figure 1d), the expected TBG moiré pattern with moiré wavelength λ_m of ∼1.1 nm becomes visible. Consequently, we observe two sets of moiré patterns: one from TBG and the other from G/hBN. These distinct moiré patterns with their characteristic periodicity become much more visible as θ_{TBG} reaches 4.87° (Figure 2c, corresponding to region 4 in Figure 1d) and the regime with a twist angle of 3.65° (see section 2 of the Supporting Information).

Remarkably, as θ_{TBG} is tuned to <2°, it becomes difficult to distinguish the two sets of moiré patterns individually. Instead, a strong hybridization between TBG and G/hBN emerges, resulting in a new type of moiré lattice structure. This is best visualized in Figure 2d, where θ_{TBG} reaches 1.89° while $\theta_{G/hBN}$ remains close to 0°. In this case, we observe periodic hexagonal moiré patterns with intensified signal hot spots (high current) at the intersections of the six corners. In addition, a central hot spot corresponding to the AAA stacking order appears within the hexagonal moiré lattice.[7] These beating hot spots form a new set of periodic moiré structures, a manifestation of strong

https://doi.org/10.1021/acs.nanolett.4c02841
Nano Lett. 2024, 24, 11490−11496

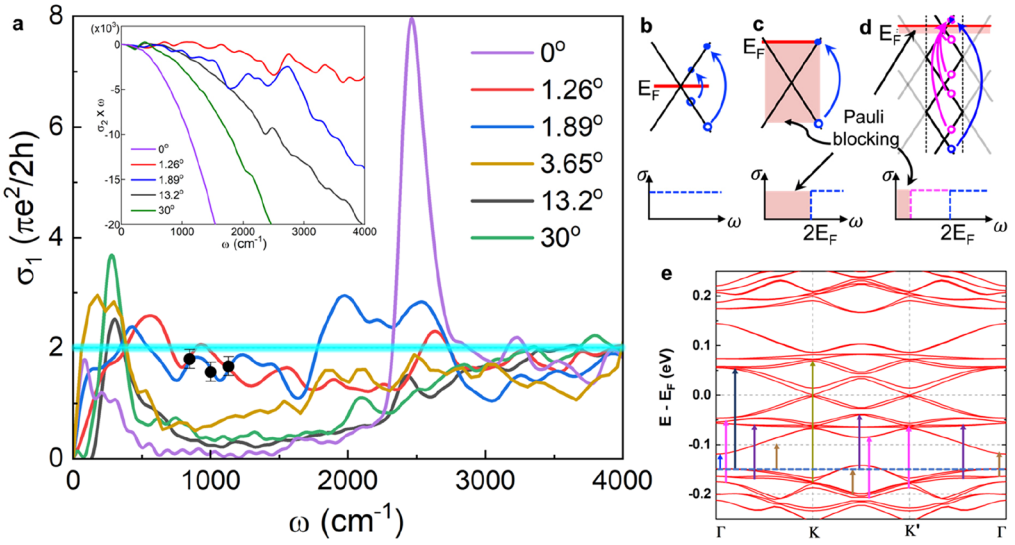

Figure 4. Superlattice-enhanced optical conductivity of a TBG/hBN double-moiré system. (a) Theoretically calculated optical conductivity spectra $\sigma_1(\omega)$ for TBG/hBN as a function of θ_{TBG} and frequency ω. The black dots highlight the experimental results that match well with the calculated optical conductivity. The inset illustrates the product of $\sigma_2(\omega)$ with frequency ω, which helps depict the redistribution of spectral weight at varying TBG twist angles. (b–d) Schematic depiction of the mechanism behind superlattice-enhanced optical conductivity. In panels b and c, we show the optical processes permitted in a Dirac cone. With finite chemical potential, only transitions extending beyond the Pauli blocking energy range are permitted. Moiré BZ folding (d) bypasses this Pauli blocking, enabling multiple transitions (magenta lines). (e) Band structure for a θ_{TBG} of 1.89°. For an E_F value of 150 meV, the double-moiré potential causes various optical transitions among the band-nested flat bands responsible for the resonances shown in panel a.

lattice hybridization and relaxation effects that are clearly resolved in the real space of the TBG/hBN double-moiré system.

We have successfully reproduced the experimental trends seen in the nanocurrent imaging by employing an atomistic scale tight-binding model of the double-moiré TBG/hBN structure that takes into account lattice relaxation effects.[35−37] To map out the distribution of electronic states in real space, we calculated the local density of states (LDOS) map for various twist angles θ_{TBG} of the system.[38] This is documented in Figure 2e–h, where the calculated LDOS of TBG/hBN matches the experimental results well in Figure 2a–d. We, therefore, conclude that the nanocurrent image constitutes a direct visualization of the commensurate double-moiré state. Furthermore, we can accurately estimate the moiré periodicity directly from the nanocurrent image. For instance, given the observed double-moiré periodicity a of 7.5 nm in Figure 2d, we determine a twist angle of 1.89°. By applying the same analysis to other sample regions, we identified their respective twist angles. Figure 3a shows a summary of the multiple domains with different θ_{TBG} twist angles observed in Figures 1 and 2.

Knowing the exact twist angle in each of the TBG/hBN domains, we now proceed to quantitatively analyze the trends observed in our nano-IR imaging data. First, we average the measured near-field amplitude and phase signal within the interior of each TBG/hBN domain and plot it as a function θ_{TBG} (Figure 3b,c). In these plots, the extracted near-field signal is normalized by the signal obtained from the region in the absence of TBG (region 8 in Figure 1c) within the same FOV. The near-field amplitude ratio and phase difference exhibit nonmonotonic behavior with respect to the twist angle (Figure 3b,c). The most pronounced difference is observed when $\theta_{TBG} < 2°$, as it approaches the small θ_{TBG} twist angles. The normalized near-field contrast systematically weakens as θ_{TBG} deviates from the small twist angles and gradually recovers at much larger twist angles. This twist angle dependence of the obtained near-field signal highlights subtle yet systematic variations in the modified electronic and optical response within TBG/hBN double-moiré lattices.

We proceeded to compare the twist angle dependence of our nano-IR imaging data with theoretical calculations to gain insight into these experimental observations. Our near-field model incorporates tip–sample interactions by considering known atomic force microscope tip information, i.e., its radius and tapping amplitude. The only other input into the model is computed complex optical conductivity $\sigma(\omega)$ that describes the optical response of TBG/hBN as a function of frequency, as shown in panels b and c of Figure 3. The quantitative agreement between the calculated near-field signal and the experimental results, as depicted in panels b and c of Figure 3, provides compelling evidence for the accuracy of the modeling. Utilizing the same procedure, we have also examined the near-field amplitude and phase signals as a function of the incident light frequency in the range of 860–1100 cm^{-1}. We found that the calculated near-field signals show good agreement with the experimental data, as detailed in section 10 of the Supporting Information. This agreement serves as the cornerstone of our further analysis, enabling us to shift our focus from discussing nano-IR imaging data to examining the behavior of $\sigma(\omega)$, a conceptually more straightforward quantity to interpret that is directly linked to the electronic structure of TBG/hBN double-moiré lattices at each twist angle θ_{TBG}.

Following this line of reasoning to decipher the origin of the observed nonmonotonic near-field optical signal variation, we can now examine the optical transitions enabled by TBG/hBN double-moiré lattice potentials that give rise to complex optical conductivity $\sigma(\omega)$ (see section 7 of the Supporting Information). Figure 4a shows the real part of optical conductivity $\sigma_1(\omega)$ at a selected twist angle θ_{TBG}. One of the most striking observations is that as θ_{TBG} approaches the magic

https://doi.org/10.1021/acs.nanolett.4c02841
Nano Lett. 2024, 24, 11490−11496

angles, the optical conductivity exhibits a nearly constant value, even at finite doping levels across a wide range of mid-IR frequencies.

To understand this unique behavior of TBG's $\sigma_1(\omega)$, it is helpful to first discuss the optical conductivity of an isolated Dirac cone, as shown in panels b and c of Figure 4. The contribution to optical conductivity comes from the direct transitions between the occupied and available electronic states in different bands. With chemical potential at the Dirac point (Figure 4b), direct interband transitions are feasible at all light frequencies, resulting in the equation $\sigma(\omega) = \sigma_0 = \pi e^2/2h$, which sets a fundamental value (the normalization constant of Figure 4a). As chemical potential E_F moves away from a Dirac point (Figure 4c), interband transitions are quenched until light frequency ω exceeds $2E_F$, where direct transitions become possible again.

The band structure of TBG at small twist angles can be considered as the folding of two Dirac cone dispersions at the edge of the mBZ. This folding process effectively "duplicates" the graphene bands multiple times, displacing the copies in energy, as depicted in Figure 4d. Moreover, the formation of a TBG/hBN double moiré breaks the inversion symmetry and introduces a finite band gap into the far-IR frequencies.[17] It also lifts the band degeneracy, doubling the number of available electronic states and facilitating additional optical transitions (section 7 of the Supporting Information). The combined effect of mBZ folding in TBG and the presence of the second G/hBN moiré substantially amplifies the occurrence of interband transitions below $2E_F$ (Figure 4d). Such a mechanism bypasses the energy-momentum conservation (Pauli blocking) that would otherwise restrict transitions in a single Dirac cone (Figure 4c). Consequently, it results in a nearly universal optical conductivity in which $\sigma_1(\omega)$ approaches $2\sigma_0$, twice the optical conductivity of undoped graphene[39,40] (here the factor of 2 arises from the double Dirac cones originating from each valley in each layer).

The scenario described above withstands rigorous optical conductivity calculations using a realistic atomic tight-binding approach. The nearly quantized $\sigma_1(\omega) \sim 2\sigma_0$ of TBG was initially theoretically proposed and explained[30] as originating from transitions happening at frequencies much larger than the moiré potential (~100 meV), wherein its fingerprints on the electronic spectrum are less noticeable in $\sigma_1(\omega)$. In our experiment, the chosen light frequency effectively probes the energy landscape of moiré potential, leading to the emergence of the resonance features depicted in Figure 4a. With a θ_{TBG} of 1.89° as an example, apart from the linear dispersive bands near the Dirac cone regime (Figure 4e, from −50 to 50 meV), multiple pairs of flat and dispersive bands emerge that are spreading along moiré BZ's Γ−K, Γ−K′, and K−K′ high-symmetry directions. Specifically, the optical resonance features observed in the $\sigma_1(\omega)$ spectra (Figure 4a, blue curve) can be attributed to several threshold interband transitions at ω values of 147 cm^{-1} (blue color), 428 cm^{-1} (dark brown color), 901 cm^{-1} (purple color), 1233 cm^{-1} (magenta color), 1971 cm^{-1} (asparagus color), etc. A similar analysis for a θ_{TBG} of 1.26° has also been conducted as documented in section 6 of the Supporting Information. Through this analysis, we found that θ_{TBG} values of 1.89° and 1.26° exhibit nearly identical optical responses $[\sigma_1(\omega) \sim 2\sigma_0]$ with slight modulation due to threshold transitions in the low-energy regime (from 400 to 1500 cm^{-1}). The optical response that we observed, which appears to be insensitive to θ_{TBG} across a wide range of twist angles, contrasts starkly with the electrical transport observations. This stark difference highlights the profound impact of the double-moiré effect in TBG/hBN that effectively circumvents the Pauli blocking, as illustrated in Figure 4d. In short, these optical transitions and resonance features enhance the overall contrast due to double-moiré potential and suppress weaker plasmonic fringes, consistent with the near-field imaging data shown in Figure 1.

To validate this understanding, we also examined the cases of limiting twist angles: $\theta_{TBG} = 0°$ and θ_{TBG} values far from the magic angles. The $\theta_{TBG} = 0°$ case deviates from the scenario described above, as it corresponds to a Bernal bilayer graphene in which the sample relaxes from the energetically unfavorable AA stacking to AB stacking (see the Supporting Information for careful analysis of the $\theta_{TBG} = 0°$ case). Consequently, when $\theta_{TBG} = 0°$, apart from weak features below 300 cm^{-1}, σ_1 remains zero over a wide range of mid-IR frequencies. Accordingly, a low plasmonic contrast is expected, which is consistent with the observed nano-imaging data depicted in Figure 1c. As θ_{TBG} becomes much larger than the magic angles, the prevalence of a double-moiré-enabled optical transition gradually diminishes as fewer folded bands are present, and thus, Pauli blocking restricts a larger number of states. Hence, we anticipate an intermediate $\sigma_1(\omega)$ that is larger than that of the $\theta_{TBG} = 0°$ case but weaker than that of θ_{TBG} at small twist angles. These observations align with our experimental results, as demonstrated in Figure 3b.

In short, our findings show that TBG/hBN structures with small twist angles ($\theta_{TBG} < 2°$) exhibit nearly universal optical conductivity across a wide frequency range, resulting in mid-IR transparency. Importantly, this unique behavior does not necessitate specific doping levels or magic angles, highlighting the significance of the moiré superlattice in shaping the optoelectronic properties of the TBG/hBN double moiré. Furthermore, we have successfully employed a combination of nano-IR and nanocurrent imaging techniques to locally probe the electronic structure and optical responses of TBG/hBN through the nanoplasmonic channel. This approach provides valuable insights into the unique optoelectronic characteristics of moiré materials at the nanoscale. Moreover, our nanocurrent study at a θ_{TBG} of 1.89° highlights one of the first observations in the TBG/hBN double moiré with a commensurate moiré wavelength of ~7.5 nm, which is the half-integer instead of integer relationship with a G/hBN moiré wavelength of ~14 nm. Our experimental observations thus indicate the profound impact of geometric relaxations in double-moiré lattices, which is likely to trigger intriguing new phenomena for producing desirable optical properties and is likely to pave the way for innovative advancements in moiré optoelectronics. Future experimental works at lower temperatures and frequencies in the far-IR range[41] and terahertz for such double-moiré materials are expected to open up exciting opportunities to explore a wide range of intriguing theoretical predictions,[42−44] while leveraging the capabilities of nanoplasmonics as a unique local-optical probe for investigating collective electronic phenomena.

■ ASSOCIATED CONTENT

Supporting Information

The Supporting Information is available free of charge at https://pubs.acs.org/doi/10.1021/acs.nanolett.4c02841.

https://doi.org/10.1021/acs.nanolett.4c02841
Nano Lett. 2024, 24, 11490−11496

Detailed description of TBG/hBN device fabrication and characterization, determination of domains and TBG twist angles, plasmon signal simulation and line profile fitting, tight binding calculations of the TBG/hBN band structure at variable twist angles, analysis of the optical transition and optical conductivity, discussion of interband and intraband contributions, frequency dependence analysis of the near-field signal, and analysis of the lattice relaxation effects (PDF)

AUTHOR INFORMATION

Corresponding Authors

Haomin Wang − *State Key Laboratory of Materials for Integrated Circuits, Shanghai Institute of Microsystem and Information Technology, Chinese Academy of Sciences, Shanghai 200050, P. R. China;* orcid.org/0000-0001-6388-2432; Email: hmwang@mail.sim.ac.cn

Guangxin Ni − *Department of Physics, Florida State University, Tallahassee, Florida 32306, United States; National High Magnetic Field Laboratory, Tallahassee, Florida 32310, United States;* orcid.org/0000-0002-7216-1829; Email: guangxin.ni@magnet.fsu.edu

Authors

Songbin Cui − *Department of Physics, Florida State University, Tallahassee, Florida 32306, United States; National High Magnetic Field Laboratory, Tallahassee, Florida 32310, United States*

Chengxin Jiang − *State Key Laboratory of Materials for Integrated Circuits, Shanghai Institute of Microsystem and Information Technology, Chinese Academy of Sciences, Shanghai 200050, P. R. China*

Zhen Zhan − *Key Laboratory of Artificial Micro- and Nano-structures of Ministry of Education and School of Physics and Technology, Wuhan University, Wuhan 430072, China; IMDEA Nanoscience, Faraday 9, 28049 Madrid, Spain*

Ty Wilson − *Department of Physics, Florida State University, Tallahassee, Florida 32306, United States; National High Magnetic Field Laboratory, Tallahassee, Florida 32310, United States*

Naipeng Zhang − *Department of Physics, Florida State University, Tallahassee, Florida 32306, United States; National High Magnetic Field Laboratory, Tallahassee, Florida 32310, United States*

Xiaoming Xie − *State Key Laboratory of Materials for Integrated Circuits, Shanghai Institute of Microsystem and Information Technology, Chinese Academy of Sciences, Shanghai 200050, P. R. China;* orcid.org/0000-0002-9891-6927

Shengjun Yuan − *Key Laboratory of Artificial Micro- and Nano-structures of Ministry of Education and School of Physics and Technology, Wuhan University, Wuhan 430072, China; Wuhan Institute of Quantum Technology, Wuhan 430206, China;* orcid.org/0000-0001-6208-1502

Cyprian Lewandowski − *Department of Physics, Florida State University, Tallahassee, Florida 32306, United States; National High Magnetic Field Laboratory, Tallahassee, Florida 32310, United States*

Complete contact information is available at: https://pubs.acs.org/10.1021/acs.nanolett.4c02841

Author Contributions

S.C., C.J., and Z.Z. contributed equally to this work. G.N. conceived the ideas and designed the experiments. G.N. performed the nanoscale infrared measurements and characterizations with the help of S.C., T.W., and N.Z. C.J. and H.W. synthesized the crystal and performed the c-AFM measurements. Z.Z. and S.Y. performed the tight-binding calculations. G.N. and C.L. performed theoretical analysis and near-field modeling of the data. G.N. and C.L. co-wrote the manuscript with input from all co-authors.

Notes

The authors declare no competing financial interest.

ACKNOWLEDGMENTS

G.N. acknowledges discussions with O. Vafek, P. McGoron, K. Xiao, and J. Wang. The research of near-field nano-optical imaging studies is supported by the U.S. Department of Energy (DOE) Early Career Research Program, Office of Science, Basic Energy Sciences (BES), under Grant DE-SC0022022 (G.N.). Investigation of two-dimensional polaritonics is supported by the National Science Foundation (NSF) CAREER award (DMR-2145074 to G.N.). G.N. acknowledges the support of the American Chemical Society Doctoral New Investigator (PRF# 66465-DNI10) Grants Program. G.N. and C.L. also acknowledge the Start-Up Fund from Florida State University and the National High Magnetic Field Laboratory. The National High Magnetic Field Laboratory is supported by the National Science Foundation through Grant DMR-1644779 and the state of Florida. C.J. and H.W. acknowledge support from the Strategic Priority Research Program of Chinese Academy of Sciences (XDB30000000), the National Natural Science Foundation of China (91964102, 51772317, and 12004406), the National Key R&D Program of China (2022YFF0609800 and 2017YFF0206106), the Science and Technology Commission of Shanghai Municipality (20DZ2203600), the China Postdoctoral Science Foundation (BX2021331 and 2021M703338), the Shanghai Postdoctoral Excellence Program (2021515), and the Soft Matter Nanofab (SMN180827) of Shanghai Tech University. Z.Z. acknowledges support funding from the European Union's Horizon 2020 research and innovation programme under Marie Skłodowska-Curie Grant 101034431 and from the "Severo Ochoa" Programme for Centres of Excellence in R&D (CEX2020-001039-S/AEI/10.13039/501100011033). S.Y. acknowledges support funding from the National Natural Science Foundation of China (12174291) and the Natural Science Foundation of Hubei Province (Grant 2022BAA017). Tight-binding calculations presented in this paper have been performed on the supercomputing system in the Supercomputing Center of Wuhan University.

REFERENCES

(1) Bistritzer, R.; MacDonald, A. H. Moiré bands in twisted double-layer graphene. *Proc. Natl. Acad. Sci. U. S. A.* **2011**, *108*, 12233−12237.

(2) Lopes dos Santos, J. M. B.; Peres, N. M. R.; Castro Neto, A. H. Graphene Bilayer with a Twist: Electronic Structure. *Phys. Rev. Lett.* **2007**, *99*, 256802.

(3) Wong, D.; et al. Local spectroscopy of moiré-induced electronic structure in gate-tunable twisted bilayer graphene. *Phys. Rev. B* **2015**, *92*, 155409.

(4) Cao, Y.; et al. Unconventional superconductivity in magic-angle graphene superlattices. *Nature* **2018**, *556*, 43−50.

(5) Yankowitz, M.; et al. Tuning superconductivity in twisted bilayer graphene. *Science* **2019**, *363*, 1059−1064.
(6) Zhang, Y.-H.; Mao, D.; Senthil, T. Twisted bilayer graphene aligned with hexagonal boron nitride: Anomalous Hall effect and a lattice model. *Phys. Rev. Res.* **2019**, *1*, 033126.
(7) Huang, X.; et al. Imaging Dual-Moiré Lattices in Twisted Bilayer Graphene Aligned on Hexagonal Boron Nitride Using Microwave Impedance Microscopy. *Nano Lett.* **2021**, *21*, 4292−4298.
(8) Cea, T.; Pantaleón, P. A.; Guinea, F. Band structure of twisted bilayer graphene on hexagonal boron nitride. *Phys. Rev. B* **2020**, *102*, 155136.
(9) Park, J. M.; Cao, Y.; Watanabe, K.; Taniguchi, T.; Jarillo-Herrero, P. Tunable strongly coupled superconductivity in magic-angle twisted trilayer graphene. *Nature* **2021**, *590*, 249−255.
(10) Liu, X.; Zhang, N. J.; Watanabe, K.; Taniguchi, T.; Li, J. I. A. Isospin order in superconducting magic-angle twisted trilayer graphene. *Nat. Phys.* **2022**, *18*, 522−527.
(11) Sharpe, A. L.; et al. Emergent ferromagnetism near three-quarters filling in twisted bilayer graphene. *Science* **2019**, *365*, 605−608.
(12) Serlin, M.; et al. Intrinsic quantized anomalous Hall effect in a moiré heterostructure. *Science* **2020**, *367*, 900−903.
(13) Zondiner, U.; et al. Cascade of phase transitions and Dirac revivals in magic-angle graphene. *Nature* **2020**, *582*, 203−208.
(14) Wong, D.; et al. Cascade of electronic transitions in magic-angle twisted bilayer graphene. *Nature* **2020**, *582*, 198−202.
(15) Hesp, N. C. H.; et al. Observation of interband collective excitations in twisted bilayer graphene. *Nat. Phys.* **2021**, *17*, 1162−1168.
(16) Cai, J.; et al. Signatures of Fractional Quantum Anomalous Hall States in Twisted $MoTe_2$. *Nature* **2023**, *622*, 63.
(17) Ni, G. X.; et al. Plasmons in graphene moiré superlattices. *Nat. Mater.* **2015**, *14*, 1217−1222.
(18) Ni, G. X.; et al. Fundamental limits to graphene plasmonics. *Nature* **2018**, *557*, 530−533.
(19) Low, T.; et al. Polaritons in layered two-dimensional materials. *Nat. Mater.* **2017**, *16*, 182−194.
(20) Dong, Y.; et al. Fizeau drag in graphene plasmonics. *Nature* **2021**, *594*, 513−516.
(21) Zhao, W.; et al. Efficient Fizeau drag from Dirac electrons in monolayer graphene. *Nature* **2021**, *594*, 517−521.
(22) Zhang, S.; et al. Abnormal conductivity in low-angle twisted bilayer graphene. *Sci. Adv.* **2020**, *6*, No. eabc5555.
(23) Ni, G. X.; et al. Ultrafast optical switching of infrared plasmon polaritons in high-mobility graphene. *Nat. Photonics* **2016**, *10*, 244−247.
(24) Ni, G.; et al. Long-Lived Phonon Polaritons in Hyperbolic Materials. *Nano Lett.* **2021**, *21*, 5767−5773.
(25) Sunku, S. S.; et al. Photonic crystals for nano-light in moiré graphene superlattices. *Science* **2018**, *362*, 1153−1156.
(26) McLeod, A. S.; et al. Multi-messenger nanoprobes of hidden magnetism in a strained Manganite. *Nat. Mater.* **2020**, *19*, 397−404.
(27) Ni, G. X.; et al. Soliton superlattices in twisted hexagonal boron nitride. *Nat. Commun.* **2019**, *10*, 4360.
(28) Shin, J.; Park, Y.; Chittari, B. L.; Sun, J.-H.; Jung, J. Electron-hole asymmetry and band gaps of commensurate double moire patterns in twisted bilayer graphene on hexagonal boron nitride. *Phys. Rev. B* **2021**, *103*, 075423.
(29) Long, M.; et al. Electronic properties of twisted bilayer graphene suspended and encapsulated with hexagonal boron nitride. *Phys. Rev. B* **2023**, *107*, 115140.
(30) Stauber, T.; San-Jose, P.; Brey, L. Optical conductivity, Drude weight and plasmons in twisted graphene bilayers. *New J. Phys.* **2013**, *15*, 113050.
(31) Yang, X.; et al. Nanomaterial-Based Plasmon-Enhanced Infrared Spectroscopy. *Adv. Mater.* **2018**, *30*, 1704896.
(32) Wu, Y.; et al. Manipulating polaritons at the extreme scale in van der Waals materials. *Nat. Rev. Phys.* **2022**, *4*, 578−594.
(33) Yao, Z.; et al. Polariton Spectroscopy: Nanoimaging and Nanospectroscopy of Polaritons with Time Resolved s-SNOM (Advanced Optical Materials 5/2020). *Adv. Opt. Mater.* **2020**, *8*, 2070019.
(34) Basov, D. N.; Fogler, M. M.; García de Abajo, F. J. Polaritons in van der Waals materials. *Science* **2016**, *354*, aag1992.
(35) Carr, S.; et al. Relaxation and domain formation in incommensurate two-dimensional heterostructures. *Phys. Rev. B* **2018**, *98*, 224102.
(36) Yoo, H.; et al. Atomic and electronic reconstruction at the van der Waals interface in twisted bilayer graphene. *Nat. Mater.* **2019**, *18*, 448−453.
(37) Kang, J.; Vafek, O. Pseudomagnetic fields, particle-hole asymmetry, and microscopic effective continuum Hamiltonians of twisted bilayer graphene. *Phys. Rev. B* **2023**, *107*, 075408.
(38) Long, M.; et al. An atomistic approach for the structural and electronic properties of twisted bilayer graphene-boron nitride heterostructures. *npj Comput. Mater.* **2022**, *8*, 73.
(39) Falkovsky, L A. Optical properties of graphene. *J. Phys.: Conf. Ser.* **2008**, *129*, 012004.
(40) Wang, F.; et al. Gate-variable optical transitions in graphene. *Science* **2008**, *320*, 206−209.
(41) Yang, J.; et al. Spectroscopy signatures of electron correlations in a trilayer graphene/hBN moiré superlattice. *Science* **2022**, *375*, 1295−1299.
(42) Papaj, M.; Lewandowski, C. Probing correlated states with plasmons. *Sci. Adv.* **2023**, *9*, No. eadg3262.
(43) Arora, A.; Rudner, M. S.; Song, J. C. W. Quantum Plasmonic Nonreciprocity in Parity-Violating Magnets. *Nano Lett.* **2022**, *22*, 9351−9357.
(44) Westerhout, T.; Katsnelson, M. I.; Rösner, M. Quantum dot-like plasmonic modes in twisted bilayer graphene supercells. *2D Mater.* **2022**, *9*, 014004.

https://doi.org/10.1021/acs.nanolett.4c02841
Nano Lett. 2024, 24, 11490−11496